Supplementary Information
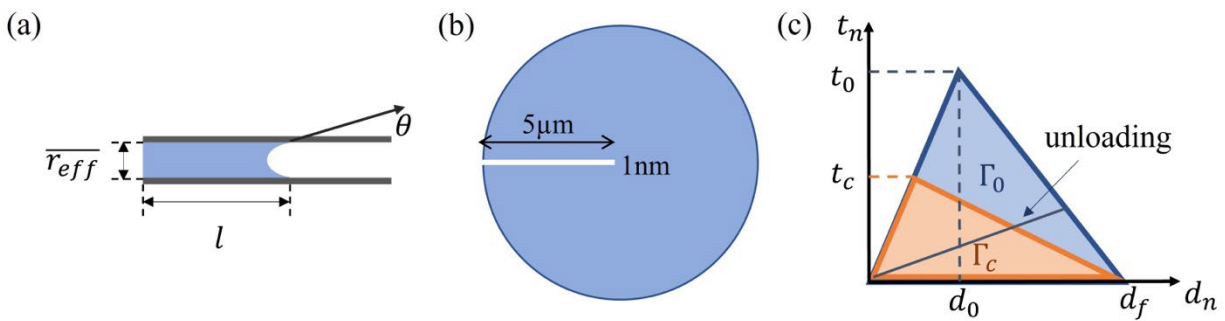

Figure S1. (a) Schematic of capillary motion. (b) Schematic showing the geometry of electrolyte infiltration inside the NMC polycrystalline particle. (c) Cohesive zone model used to model the crack initiation and growth.
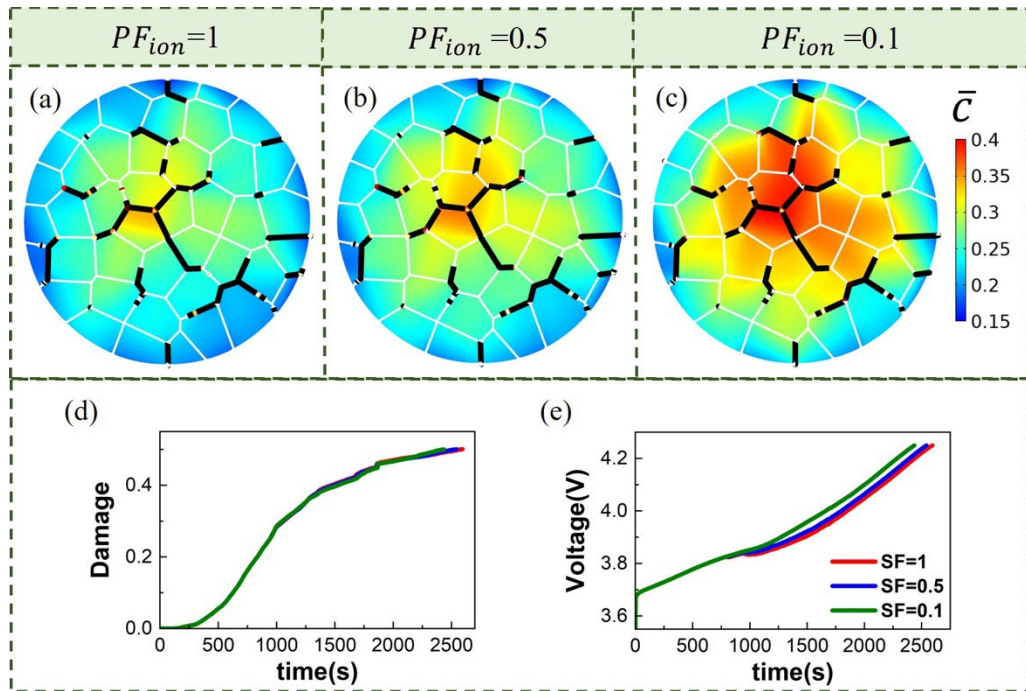
Figure S2. The parametric study of PF_{ion}. Li concentration and damage distribution at the end of the first charging are shown for (a) $PF_{ion} = 1$, (b) $PF_{ion} = 0.5$, and (c) $PF_{ion} = 0.1$. The evolution of the average damage (d) among the secondary particle and the voltage profile (e) for $PF_{ion} = 1$ (red lines), $PF_{ion} = 0.5$ (blue lines), and $PF_{ion} = 0.1$ (green lines) during the first charging process.
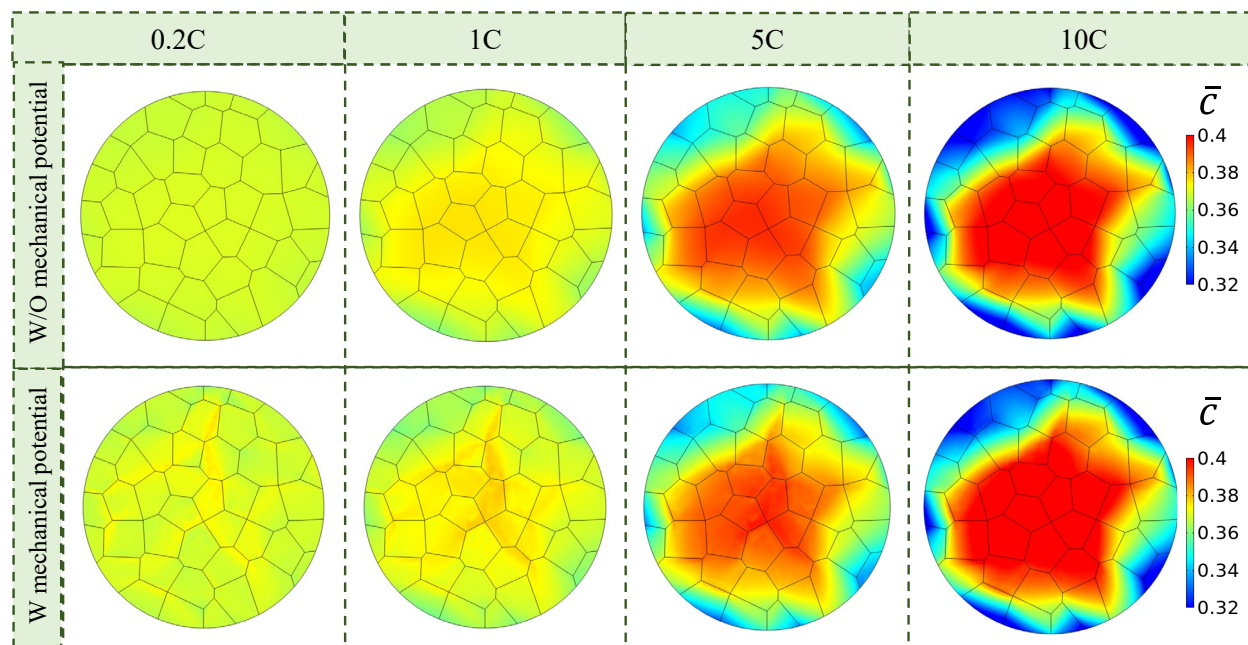
Figure S3. Comparison of Li distribution within the NMC polycrystalline particle without (upper panel) and with (lower panel) considering the mechanical potential in Li diffusion kinetics at SOC=60%. The mechanical effect is more significant at slow charging rates (0.2C and 1C), where the mechanical bias induces more heterogeneity in the Li profile. At higher C-rates (5C and 10C), the mechanical effect is minimal, and little difference is observed between the two cases.
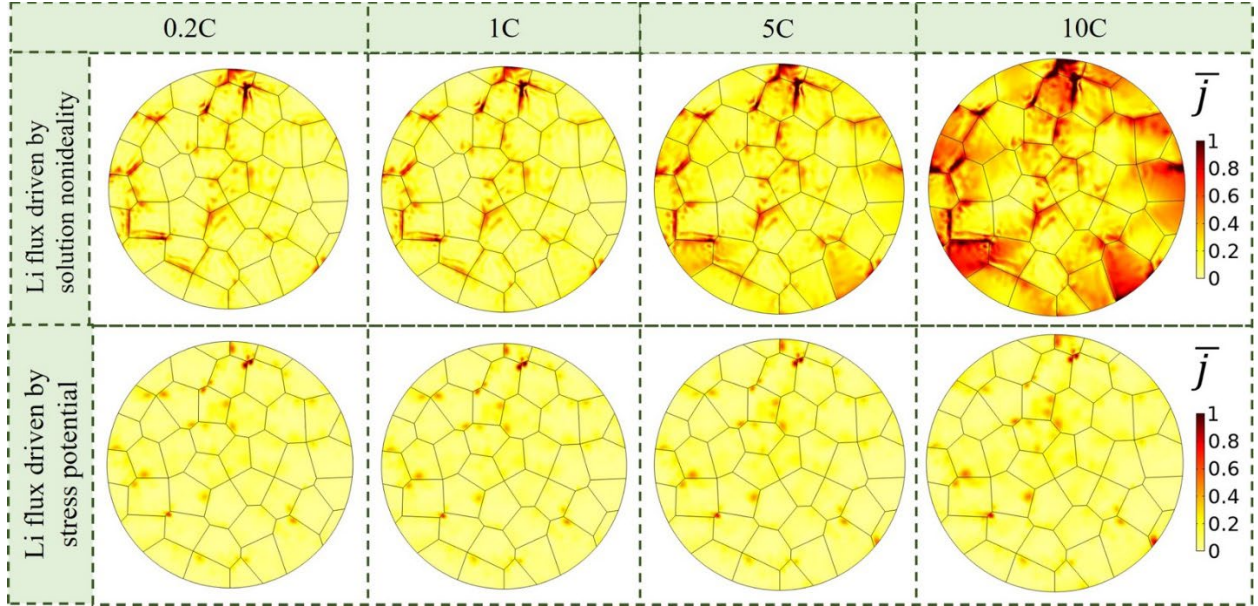
Figure S4. Comparison of Li flux driven by the solution nonideality (upper panel) and stress potential (lower panel) at multiple charging rates at SOC=60%. The contribution from the change of the mechanical stiffness is negligible and hence not plotted here. When the charging rate increases, Li flux driven by the solution nonideality drastically increases due to the higher concentration gradient within the particle. In comparison, Li flux driven by the stress potential in all the cases are in the same scale and does not show a clear trend with the increasing charging rate. Li flux contributed by the stress potential is more dependent on the materials properties, such as β_{ij}.
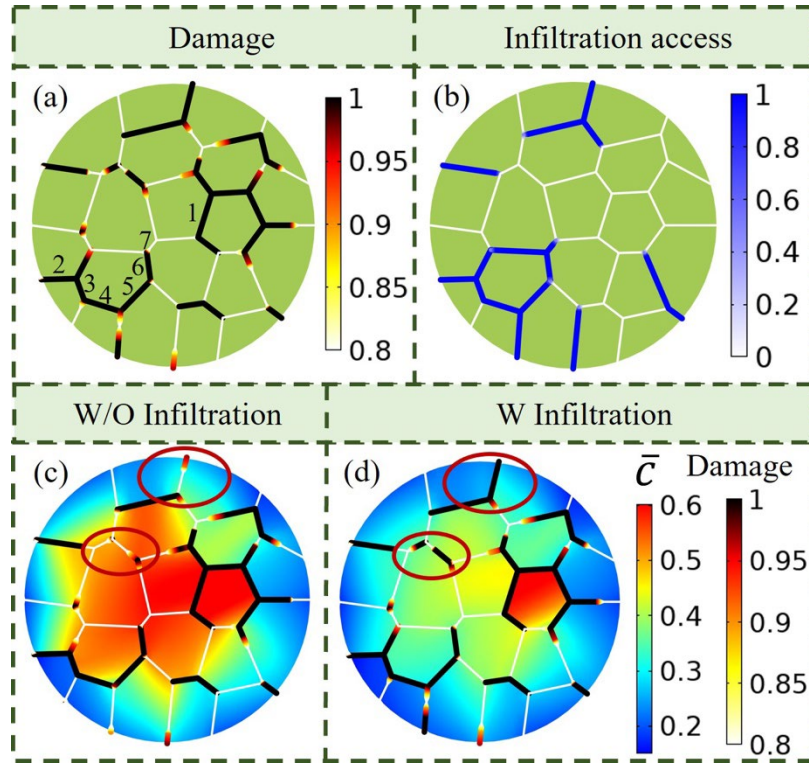
Figure S5. Numerical calibration on the electrolyte infiltration accessibility. (a) Damage profile and (b) electrolyte accessibility of the grain boundaries at the end of the first charging. Comparison between the concentration profiles and mechanical damage without considering electrolyte infiltration (c) and with electrolyte infiltration (d).

Notes: In presenting the effects of redistribution of interfacial charge transfer kinetics and corrosion due to electrolyte infiltration in Sec. 3.3, we take the assumption that the fractured grain boundaries can access to the liquid electrolyte as long as intergranular fracture initiates. However, it should be noted that if cracks initiate at the center of the particle, they may not have access to the electrolyte residing in the domain outside of the particle. Here we calibrate the electrolyte infiltration accessibility in the numerical modeling. Figure S5 (a) shows the mechanical damage within the secondary particle at the end of the first charging. In this profile, grain boundary 1 is completely damaged but is not necessarily in contact with the electrolyte because part of its

neighboring grain boundaries remains intact. Therefore, we consider 1 as a non-infiltrated grain boundary. We also note that we use a NMC secondary particle with coarser grains because the geometry is easier to compute and fine enough to illustrate the idea. We develop an algorithm in COMSOL to automatically determine the electrolyte accessibility of each grain boundary based on two criteria. First, for a given grain boundary, there should exist at least one connected pathway for the electrolyte to infiltrate. This criterion checks if the average damage of the interconnected grain boundaries is over 0.95, and thus the validation of electrolyte access. If this criterion is met, then second, the grain boundary should be fractured at the side connecting to the electrolyte transport pathway. For example, in Fig. S5 (a), grain boundary 7 is identified as electrolyte accessible because (1) the neighboring boundaries 2, 3, 4, 5, and 6 are damaged and interconnected to the particle surface, and (2) the joint between 6 and 7 is also damaged. With the above calibration of electrolyte access, we evaluate its effect of corrosion and penetration during the first charging. Fig. S5 (b) shows the accessibility of each grain boundary based on the algorithm. Only the fractured boundaries accessible to the outer surface have been recognized as electrolyte wetted surfaces. Taking boundaries 1 and 7 as an example, 1 does not have access to electrolyte from any surrounding pathway and therefore it is categorized as non-accessible, while 7 meets the accessibility criteria and liquid electrolyte can pass along. The algorithm ensures that the electrolyte infiltration effect is only implemented on the fractured boundaries accessible to the electrolyte, while non-accessible boundaries are not affected. Fig. S5 (c) and (d) show the Li concentration and damage distribution at the end of the first charging without and with considering electrolyte infiltration, respectively. We observe more cracks (shown in the red circles in Fig. S5 (c) and (d)) and less trapped Li in the model where electrolyte infiltration is incorporated. Such an

effect on Li flux and mechanical behavior of the NMC cathode is similar to the results where we do not consider the electrolyte accessibility in the main text.

Supplementary Table 1. Modeling parameters.

Parameter	Symbol	Value (unit)
Height of the porous cathode	L	20 (um)
Height of the separator	L_s	5 (um)
Width of the porous cathode	W	20 (um)
Active particle radius	r	5 (um)
Gas constant	R	8.3145 (J/(mol · K))
Temperature	T	293.15 (K)
Faraday constant	F	96485.3321 (s · A/mol)
Effective radius	$\overline{r_{\text{eff}}}$	1 (nm)
Infiltration length	l	5 (um)
Surface tension	Γ	30 (mN/m)
Contact angle	θ	5 (°)
Viscosity	ν	3 (mPa · s)
Maximum Li concentration	c_{max}	50060 (mol/m^3)
Li diffusivity along the a and b-axis	D_{ab}	2×10^{-14} (m^2/s)
Li diffusivity along the c-axis	D_c	2×10^{-15} (m^2/s)
Anodic transfer coefficient	α_a	0.5

Cathodic transfer coefficient	α_c	0.5
Rate constant for the anodic reactions	k_a	10^{-11}
Rate constant for the cathodic reactions	k_c	10^{-11}
Reference Li-ion concentration in the electrolyte	c_{ref}^l	1 (mol/m^3)
Reference current density	$i_{0_{ref}}^{sa}$	100 (A/m^2)
Original interfacial strength	t_0	200 (MPa)
Original fracture energy	Γ_0	2 (J/m^2)
Normal stiffness of the cohesive element	K_n	2×10^{17}

Notes: Electrical conductivity of carbon-binder matrix (K^c), Diffusivity of Li ions in the electrolyte (D^l), Transference number of Li^+ (t^+), Electrolyte ionic conductivity (K^l), Mean activity of the electrolyte (f) are embedded material parameters for the liquid electrolyte (LiPF6 in 1:1 EC:DEC) in COMSOL Multiphysics® (V5.6, COMSOL).

Supplementary Table 2. Fitting parameters for the open-circuit potential of NMC811.

Parameters	Unit/V
U_0	4.303
Ω_2/F	0.7261
Ω_3/F	-0.062
Ω_4/F	1.186
Ω_5/F	-1.76825
Ω_6/F	0.7256

Supplementary Table 3. Stiffness coefficients C_{ijkl} of NMC811

$Li_xNi_{0.8}Mn_{0.1}Co_{0.1}O_2$	C_{11}(GPa)	C_{12}(GPa)	C_{13}(GPa)	C_{33}(GPa)	C_{44}(GPa)
x=1	249.67	112.80	57.12	205.93	53.21
0.9	258.61	92.45	51.06	183.09	50.90
0.8	259.38	84.57	40.01	157.84	45.85
0.7	254.36	84.59	39.06	143.79	36.08
0.6	245.60	89.89	41.40	119.75	28.83
0.5	224.88	82.77	15.00	74.95	18.39
0.4	245.99	67.81	21.31	74.36	12.76
0.3	211.25	17.49	13.37	51.43	9.31